

## Observations and modeling of heat fluxes on tidal flats

J. P. Rinehimer<sup>1,2,3</sup> and Jim T. Thomson<sup>1,2</sup>

Received 18 June 2013; revised 12 November 2013; accepted 11 December 2013.

[1] A cross-shore model of tidal flat heat and mass fluxes is developed to understand the heat exchange between the sediment bed and the water column. A convective heat-transfer coefficient is used to model sediment-water heat fluxes which are as great as 20% of the incoming solar shortwave radiation. The model results match well with observations and are used to assess processes across tidal to seasonal time scales. During the summer, tidal flat sediments store incoming shortwave radiation during exposure and act effectively as a net source of heat to the water column. This pattern changes in the winter, when the flats cool during exposure and act effectively as a net sink of heat. Additionally, during the summer water temperatures at the edge of the flooding front are elevated 5°C above the surface sediment temperatures. Model results replicate this process only when water column light extinction coefficients are high, consistent with visual observations of high turbidity (and thus high light absorption) at the leading edge of the flooding front.

**Citation:** Rinehimer, J. P., and J. T. Thomson (2014), Observations and modeling of heat fluxes on tidal flats, *J. Geophys. Res. Oceans*, 119, doi:10.1002/2013JC009225.

### 1. Introduction

[2] Tidal flats occur in regions of significant sediment supply and are a common feature of estuaries and coastlines worldwide. Characterized by large intertidal areas with strong tidal forcing relative to wave forcing, these regions contain high levels of benthic microalgal biomass and production, which supply the base of coastal food webs [Colijn and de Jonge, 1984]. Tidal flats are important habitats for migratory birds, commercially valuable young fishes such as salmon, and highly productive bivalve fisheries. Tidal flats also present significant navigational hazards for ships entering coastal ports and provide much of the area for land reclamation projects.

[3] While much research has been focused on tidal flat hydrodynamics, sediment transport, and morphodynamics [see Amos, 1995; Friedrichs, 2012, for reviews], the thermodynamics of these systems are not as well understood. Water temperatures often control rates of biogeochemical processes like nutrient cycling and primary productivity [Guarini et al., 1997]. Alternating inundation and exposure of large regions of tidal flats suggest that differences between the thermodynamic properties of water and sedi-

ments may also play an important role in local climate and weather [Cho et al., 2000]. An understanding of the local heat budgets of these systems is also important when determining the impacts of significant sources of thermal pollution such as nuclear power facilities [Yanagi et al., 2005].

[4] Solar radiation represents the most important external forcing of tidal flat temperatures. Losordo and Piedrahita [1991] developed a numerical model to study the thermal structure of aquaculture ponds. During the spring, incident solar radiation heated the lake surface resulting in thermal stratification. There was sufficient mixing within the lake, however, such that heat exchange between the sediment and water column was important in determining the thermal budget. Warm water was mixed from above and the sediment bed acted as a net sink of heat. This was reversed during the fall when diminished solar radiation and lower air temperatures resulted in the mixing of cold water to depth and the loss of heat from the sediment bed to the water column.

[5] Similar seasonal cycles are apparent on tidal flats as well as in aquaculture ponds. Kim et al. [2010] found that during spring local solar heating of exposed tidal flats in Baeksu, Korea caused temperature differences of 2–4°C between the sediment surface and water column temperatures. Inversely, during the winter and limited incident solar radiation, exposed sediment temperatures were lower than water column temperatures with the coldest seawater temperatures occurring in the shallow regions of the embayment. These differences between the sediment and water column temperatures create thermal gradients that drive heat exchange between the seabed and water column. Net heat transfer between the water and the sediment is thus determined by the phasing of solar shortwave radiation and periods of exposure of the tidal flats.

[6] The study of Kim et al. [2010] used a similar method to that of Losordo and Piedrahita [1991] to calculate the

<sup>1</sup>Applied Physics Laboratory, University of Washington, Seattle, Washington, USA.

<sup>2</sup>Department of Civil and Environmental Engineering, University of Washington, Seattle, Washington, USA.

<sup>3</sup>Now at Center for Coastal Margin Observation and Prediction, Oregon Health and Sciences University, Portland, Oregon, USA.

Corresponding author: J. P. Rinehimer, Applied Physics Laboratory, University of Washington, 1013 NE 40th St., Seattle, WA 98105, USA. (jprine@apl.washington.edu)

net heat flux between the sediment bed and the water column. They assume an effective sediment thickness ( $H_{sed}$ ) over which heat exchange occurs to calculate the net sediment-water heat flux, following:

$$Q_{sw} = C_s \frac{2\kappa}{H_{sed}} (T_w - T_s) \quad (1)$$

where  $Q_{sw}$  is the sediment-water heat exchange,  $T_w$  is the water temperature,  $T_s$  is the sediment surface temperature,  $H_{sed}$  is the “effective” sediment thickness, and  $\kappa$  and  $C_s$  are the thermal diffusivity and volumetric specific heat capacity of the seabed. *Kim et al.* [2010] do not report their values of  $H_{sed}$  nor whether they vary over seasonal time scale or remain constant. While the effective thickness approach seems to be reasonable for sediments that are always inundated and rarely disturbed, it may be inappropriate for shallow tidal flat regions that experience exposure and inundation.

[7] These prior studies also required the specification of sediment temperatures at depth in order to accurately replicate their observations. Given that these data may not be available in all cases and, over spring-neap time scales, surface heat exchange and seawater advection represent the primary sources of heat to tidal flat sediment and waters, reasonably accurate predication of tidal flat temperatures should be possible without knowledge of the sediment temperature at depth.

[8] This study adapts the previous work and aims to improve thermodynamic process modeling for tidal flats. The results of in situ measurements and modeling studies are described at two locations: Skagit Bay and Willapa Bay, Washington, USA during summer and winter 2009. The field data are used to calibrate and force a one-dimensional, cross-flat model of tidal flat mass and heat fluxes including heat exchange between the tidal flat sediment and the water column. Times scales of seasonal, fortnightly, and tidal variations are addressed. Estimates of net sediment-water heat fluxes for each season are determined and the sensitivity of the fluxes to sediment and water parameters is evaluated. Small-scale heating processes at the flooding front are then examined to determine local heating during the summer months.

## 2. Methods

### 2.1. Study Sites and Field Observations

[9] Field observations and model calculations were performed for two tidal flats in Washington State, USA: Skagit Bay and Willapa Bay (Figure 1). Willapa Bay is a bar-built embayment on the Pacific Coast with a tidal range varying from 1.8 to 3.7 m between neap and spring tides. Nearly half of the bay’s surface area is intertidal [*Andrews*, 1965]. The study sites are located in the southern portion of Willapa Bay in sediments consisting of primarily silt and clay [*Boldt et al.*, 2013]. Skagit Bay, located 230 km to the northeast of Willapa Bay, is a subembayment of Puget Sound and the receiving basin for the Skagit River. Sediment deposits at the mouth of the Skagit River form a large intertidal delta with sand occurring nearshore and grain size fining southwestward, away from the mouth. Fine-grained sediments are also located in sheltered areas north

of the Swinomish Channel [*McBride et al.*, 2006]. The neap-spring tidal range varies from 2.5 to 5 m.

[10] Sediment and water temperature observations were collected at both bays spanning a (noncontinuous) period of 2 years (2009–2010). Hobo TempPro v2 temperature loggers affixed to a metal sand anchor recorded temperatures in the sediment bed, spaced at 10 cm intervals spanning 10–50 cm depths in the sediment. At the sediment surface, a Hobo U20 water level logger measured water depth and surface temperatures. An additional TempPro logger attached to a length of nylon rope measured near-bed water temperatures during inundation at 10 cm above the sediment surface. The temperature loggers recorded at 5 min intervals, over twice the response time of the loggers, and have an accuracy of  $\pm 0.2^\circ\text{C}$  with a resolution of  $0.02^\circ\text{C}$ . Prior studies by *Thomson* [2010] have shown minimal effects due to heat conduction down the sand anchor and disturbance of the sediment bed during deployment with a RMS deviation of  $< 0.15^\circ\text{C}$  between plastic and metal sand anchors. This variance is small compared to the  $\pm 10^\circ\text{C}$  variations seen in the daily temperatures.

[11] A HOBO U30 meteorological station located near the study sites collected 5 min observations of air temperature, wind speed and direction, solar shortwave radiation, and relative humidity. The meteorological station was attached to a 1.5 m tripod and located on the nearby Craft Island at 28 m elevation while at Willapa Bay it was affixed to a piling near Round Island at 7 m elevation. Nearby Washington State University AgWeatherNet stations at Long Beach (Willapa Bay) and Fir Island (Skagit Bay) were used to provide meteorological data during brief data gaps. Hourly METAR reports from nearby airports in Astoria, OR (KAST) and Burlington, WA (KBVS) provided observations of cloud cover. As METAR observations report cloud cover values in oktas at various elevations, the maximum okta value over all reported elevations for each hourly report was used to determine the percent cloud cover.

### 2.2. Numerical Model

[12] A one-dimensional (cross-flat) numerical model, following *Kim et al.* [2010], was developed to simulate the tidal wetting and drying of the flats and the heat fluxes to the water and sediment. The model considers horizontal, cross-flat advection of mass and heat as well as the vertical diffusion of heat in the sediment bed. The cross-flat resolution is 50 m and the water column is represented by a single, vertically homogenous cell at each cross-flat location. *Pavel et al.* [2012] indicate that some stratification occurs on the flats, however, it is generally intermittent, occurring when the leading edge of the flood or ebb tidal front pass over the site. Mass and heat fluxes are assumed to be dominated by advective processes and cross-flat diffusion is not modeled. Along flat processes are also ignored. Model bathymetry  $H^i$  is assigned according to the average slope of the flats, about 0.79 m/km at Skagit Bay and 0.76 m/km at Willapa Bay. The offshore boundary depth was  $-5$  m (MLLW) for each site.

#### 2.2.1. Water Column Model

[13] The model is forced at the open boundary by a tidally varying sea surface elevation  $\eta_t$ . Assuming a constant water elevation over the modeled domain allows calculation of the mass flux and velocity using only the continuity equation

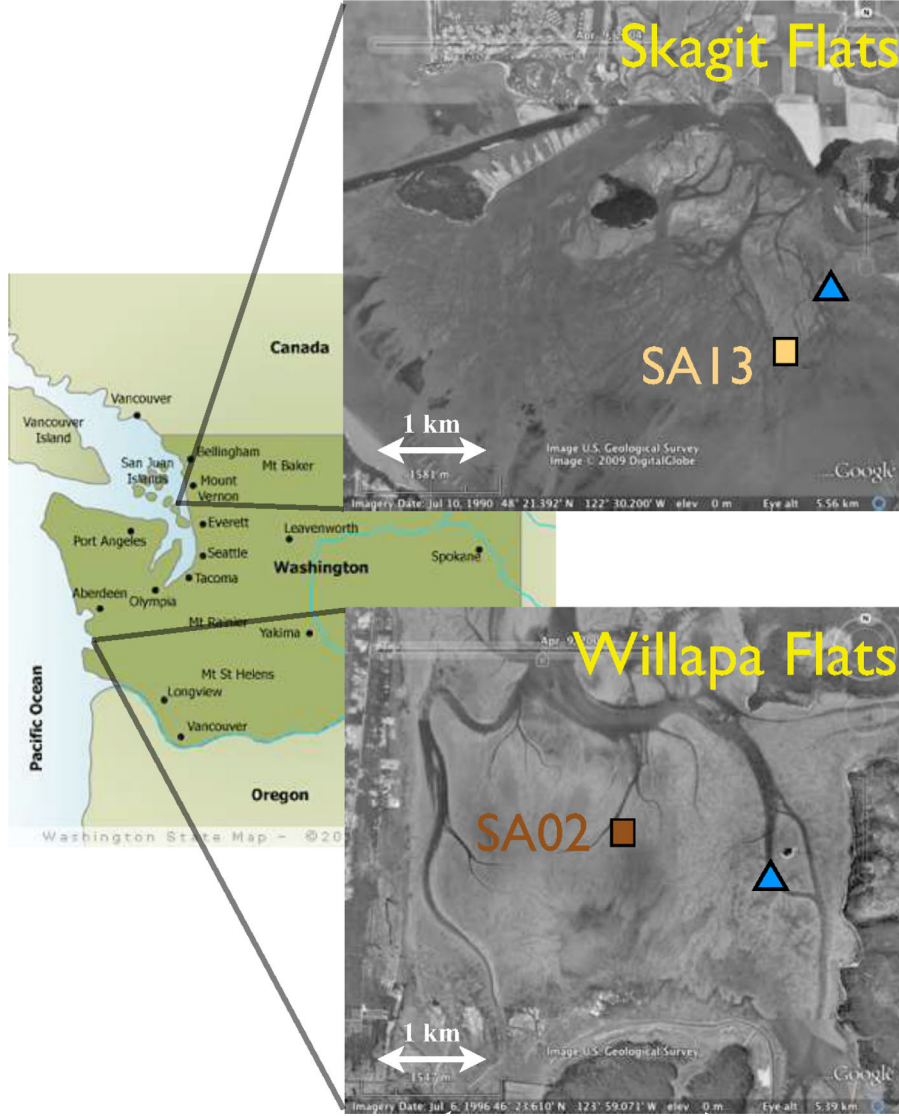


**Figure 1.** Location of field observations at Skagit Bay and Willapa Bay, WA, USA. Squares indicate the sand anchor locations at each site. Triangles are the locations of the HOBO Met station. Figure modified from Thomson [2010].

$$F_i^i = \sum_{k=i}^M \left( \frac{\eta_t - \eta_{t-\Delta t}}{\Delta t} \right) dx \quad (2)$$

where  $F_i^i$  is the volume flux between cells  $i-1$  and  $i$  at time  $t$ ,  $\Delta t$  is the time step size,  $dx$  is the horizontal cell size, and  $M$  is the total number of cross-channel cells in the domain. No fluxes are permitted through the onshore boundary. Subscripts indicate time indices, while superscripts indicate spatial indices.

[14] The water temperature  $T_{w,t}^i$  at location  $i$  and time  $t$  is calculated by

$$T_{w,t}^i = \frac{H^i + \eta_{t-\Delta t}}{H^i + \eta_t} T_{w,t-\Delta t}^i + \Delta T_{adv} + \Delta T_{ext} \quad (3)$$

where the first term is the previous temperature accounting for changes in cell size (i.e., water elevation),  $\Delta T_{adv}$  is due to the advective heat flux, and  $\Delta T_{ext}$  is due to the external

heat fluxes through the water surface or sediment-water interface. The local and external terms are calculated through first order, backward differences (in time) as

$$\Delta T_{ext} = \frac{Q_{w,t}^i \Delta t}{C_w (H^i + \eta_t)} \quad (4)$$

where  $C_w$  is the volumetric heat capacity of water and  $Q_{w,t}^i$  is the net heat flux into the water column (see below).

[15] The advective term depends on the flow direction and is determined by

$$\Delta T_{adv} = \begin{cases} \left( T_{w,t-\Delta t}^{i-1} F_t^i - T_{w,t-\Delta t}^i F_t^{i+1} \right) \frac{\Delta t}{dx (H^i + \eta_t)} & \text{during flood} \\ \left( T_{w,t-\Delta t}^i F_t^i - T_{w,t-\Delta t}^{i+1} F_t^{i+1} \right) \frac{\Delta t}{dx (H^i + \eta_t)} & \text{during ebb} \end{cases} \quad (5)$$

[16] At the open boundary, an offshore water temperature  $T_{sea}$  is specified while no fluxes occur through the landward boundary.

### 2.2.2. Sediment Model

[17] Vertical transport of heat within the sediment bed is modeled at each  $x$  location according to the diffusion equation

$$\frac{dT}{dt} = \kappa \frac{d^2T}{dz^2} \quad (6)$$

where  $\kappa$  is the thermal diffusivity of the sediment and  $T_s$  is the sediment temperature, which varies with depth. The diffusion equation is solved at each modeled cross-flat location and no horizontal mixing is allowed between locations. Equation (6) is modeled using a second-order Rung-Kutta method. The lower boundary condition assumes that  $dT/dz$  is constant with the layer above, while the boundary at the surface interface is given by

$$Q_s = \lambda_s \left. \frac{dT}{dz} \right|_{z=0} \quad (7)$$

where  $Q_s$  is the heat flux through the surface and  $\lambda_s$  is the thermal conductivity of the sediment. The bed is modeled from the surface down to 2 m depth with 10 cm vertical resolution.

[18] Thermal diffusivity  $\kappa$  and conductivity  $\lambda_s$  depend on the sediment type, porosity, and water content [Thomson, 2010]. Kim *et al.* [2007] summarize prior studies with values of  $\kappa$  between 0.4 and  $1.1 \times 10^{-6} \text{ m}^2 \text{ s}^{-1}$  and  $\lambda$  between 0.8 and  $3.1 \text{ W m}^{-1} \text{ K}^{-1}$ . For this study,  $\kappa = 1.0 \times 10^{-6} \text{ m}^2 \text{ s}^{-1}$  was chosen for the Skagit Bay site and  $\kappa = 0.5 \times 10^{-6} \text{ m}^2 \text{ s}^{-1}$  was chosen for Willapa Bay based on Thomson [2010] which found values of  $\kappa$  between 0.6 and  $1.4 \times 10^{-6} \text{ m}^2 \text{ s}^{-1}$  for Skagit Bay sand and 0.4 and  $0.6 \times 10^{-6} \text{ m}^2 \text{ s}^{-1}$  for Willapa Bay mud. A range of conductivities between  $\lambda = 1-10 \text{ W m}^{-1} \text{ K}^{-1}$  [Thomson, 2010] were used to tune the model and test sensitivity.

### 2.2.3. Heat Fluxes

[19] The net heat flux into the water column ( $Q_w$ ) or the sediment ( $Q_s$ ) is determined by

$$Q_w = Q_{ws} + Q_{wl} + Q_{wh} + Q_{we} + Q_{sw} \quad (8)$$

$$Q_s = Q_{ss} + Q_{sl} + Q_{sh} + Q_{se} - Q_{sw} \quad (9)$$

where  $Q_{xs}$  is the net shortwave radiation,  $Q_{xl}$  is the net longwave radiation,  $Q_{xh}$  is the sensible heat flux,  $Q_{xe}$  is the latent heat flux, and the first subscript  $x$  indicates whether the flux is to the sediment ( $s$ ) or the water column ( $w$ ). Figure 2 shows a schematic diagram of each of these fluxes within the context of a tidal flat. Solar shortwave radiation is calculated according to

$$Q_{sn} = (1 - \alpha_x) Q_{s0} \quad (10)$$

where  $Q_{s0}$  is the incoming shortwave radiation,  $Q_{sn}$  is the net shortwave radiation, and  $\alpha_x$  is the albedo of the appropriate substance. Despite seasonal variations in albedo due to changing solar angle [Kim *et al.*, 2007], constant mean

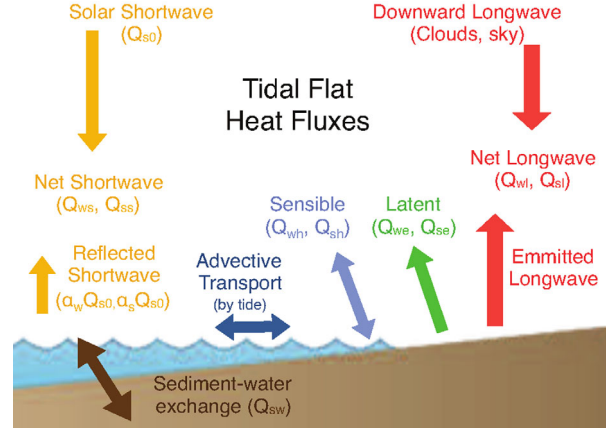


**Figure 2.** Schematic diagram of heat fluxes on tidal flats. Arrows indicate the direction of heat flux. See section 2.2.3. for a description of the various terms.

values of  $\alpha_s = 0.20$  and  $\alpha_w = 0.05$  were used for the model [Thomson, 2010].

[20] During exposure of the flats, all net shortwave radiation is absorbed by the sediment bed such that  $Q_{ss} = Q_{sn}$ . During inundation, however, not all of the net radiation is absorbed by the water, and some of the incident solar shortwave radiation may reach the seabed. The fraction of radiation that reaches the bed can be computed by the Beer-Lambert law:

$$T = e^{-K_d d} \quad (11)$$

where  $d$  is the depth,  $T$  is the transmissivity, and  $K_d$  is the extinction coefficient. The amount of shortwave radiation that is absorbed by the water column is  $Q_{ws} = (1 - T)Q_{sn}$  and the seabed  $Q_{ss} = TQ_{sn}$ . The extinction coefficient varies as a function of wavelength, with longer wavelength radiation generally having higher extinction coefficients [Jerlov, 1976]. Extinction coefficients of  $1-25 \text{ m}^{-1}$  are common for moderate turbidities from 10 to  $100 \text{ mg L}^{-1}$  within the 400–700  $\mu\text{m}$  photosynthetically active radiation (PAR) range [Stefan *et al.*, 1983]. Nearly half of the solar shortwave radiation is outside this range, however, and within the more quickly attenuating IR range. Studies of the Hudson River plume indicate values of  $K_d > 100 \text{ m}^{-1}$  within the plume [Cahill *et al.*, 2008]. For this study, a bulk value for all wavelengths will be used to estimate the qualitative impacts of absorption coefficient.

[21] The longwave heat flux,  $Q_{xl}$  is calculated following May [1986]

$$Q_{xl} = \left[ \epsilon \sigma T_a^4 \left( 0.4 - 0.05 e_a^{1/2} \right) + 4 \epsilon \sigma T_a^3 (T_x - T_a) \right] \cdot (1 - 0.75 C^{3.4}) \quad (12)$$

where  $\epsilon$  is the emissivity,  $\sigma$  is the Stefan-Boltzmann constant ( $5.6705 \times 10^{-8} \text{ W m}^{-2} \text{ K}^{-4}$ ),  $T_a$  is the air temperature,  $C$  is the fractional cloud cover from 0 to 1,  $e_a$  is the vapor pressure of air above the tidal flat, and  $T_x$  is the water temperature  $T_w$  or the sediment surface temperature  $T_s$ .

[22] Calculation of sensible heat transfer,  $Q_{xh}$  is given by Guarini *et al.* [1997]:

$$Q_{xh} = \rho_a C_{Pa} C_h (1+U)(T_x - T_a) \quad (13)$$

where  $\rho_a$  is the density of air,  $C_{Pa}$  is the specific heat of air at standard pressure,  $C_h$  is the bulk transfer coefficient for conduction, and  $U$  is the wind speed in m/s.

[23] Latent heat transfer,  $Q_{xe}$  is given following Guarini *et al.* [1997]:

$$Q_{se} = \xi V_s \quad (14)$$

$$Q_{we} = V_w \quad (15)$$

where  $\xi$  is the fractional water content of the flat surface with  $V_s$  and  $V_w$  defined as:

$$V_x = \rho_a L_V C_v (1+U)(q_x - q_a) \quad (16)$$

$$L_V = [2500.84 - 2.35(T_x - 273.15)] \times 10^3 \quad (17)$$

$$q_s = \frac{\lambda p_{sat}^V}{p_{atm} - (1-\lambda)p_{sat}^V} \quad (18)$$

$$p_{sat}^V = \exp \left\{ 2.3 \left[ \frac{7.5(T_x - 273.15)}{237.3 + (T_x - 273.15)} + 0.76 \right] \right\} \quad (19)$$

where  $\rho_a$  is the density of air ( $1.29 \text{ kg m}^{-3}$ ),  $C_v$  is the bulk transfer coefficient for conduction (0.0014),  $U$  is the wind speed ( $\text{m s}^{-1}$ ) at 10 m,  $L_V$  is the latent heat of evaporation,  $q_s$  is the specific humidity of saturated air at the (pore) water temperature,  $q_a$  is the absolute air humidity,  $p_{atm}$  is the atmospheric pressure, and  $p_{sat}^V$  is the saturation vapor pressure.

[24] The heat flux through the sediment-water interface is denoted by  $Q_{sw}$  where positive values indicate heat flux to the water column and negative values indicate heat flux to the sediment. The sediment-water heat flux is estimated using a convective heat-transfer coefficient  $h_{sw}$  [Incropera and DeWitt, 2002]:

$$Q_{sw} = h_{sw}(T_s - T_w) \quad (20)$$

[25] Previous studies [Kim *et al.*, 2010; Losordo and Piedrahita, 1991] have used a formulation of  $Q_{sw}$  which requires the determination of an effective sediment thickness, however, no guidance for the determination this parameter is presented. The alternative used here, a heat-transfer coefficient, is common in convective transfer between a fluid and a solid [Incropera and DeWitt, 2002] and is straightforward to estimate empirically.

[26] Estimations of  $h_{sw}$  were obtained by the ‘‘heat storage’’ method [Harrison, 1985]. To determine the change in heat content of the sediment bed, observations of sediment temperature with depth were integrated vertically according to:

$$Q_{sw} = \frac{\partial}{\partial t} \int_{z_0}^0 C_v T(z) dz + \lambda_s \frac{\partial T}{\partial z} \Big|_{z_0} \quad (21)$$

where  $C_v$  is the volumetric heat capacity of the sediment bed,  $\lambda_s$  is the thermal conductivity of the sediment, and  $z_0$  is the depth of integration into the bed. The first term of the right-hand side of equation (21) represents the change in

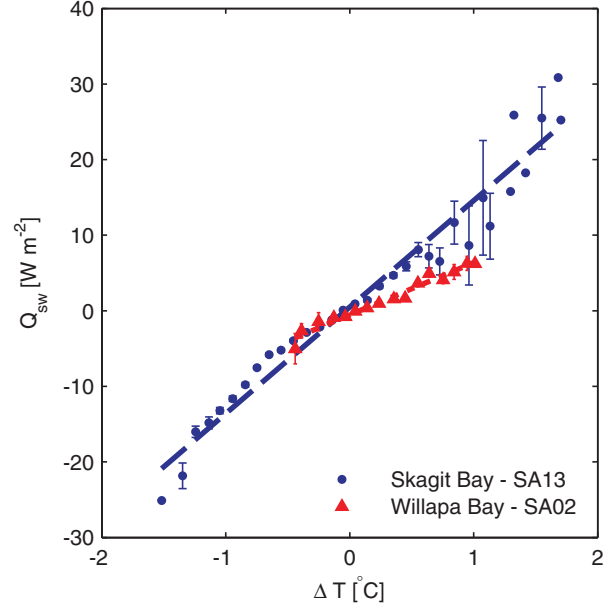


**Figure 3.** Example fit for  $h_{sw}$  for Skagit Bay (SA13) and Willapa Bay (SA02).  $Q_{sw}$  is the heat difference as calculated by equation (21) and  $\Delta T = (T_{sed} - T_w)$ . Data have been binned into  $0.1^\circ\text{C}$  intervals with the vertical error bars showing the standard error in  $dQ$  for each bin.

storage of heat in the upper portion of the sediment bed while the second term represents the flux of heat into the lower layers.  $z_0 = 0.5 \text{ m}$  was taken as the lowest elevation of the sediment temperature measurements. Equation (21) was discretized by a forward difference in time and a backward difference at  $z = z_0$  to estimate heat transfer below  $z_0$ .  $h_{sw}$  was then estimated by combining equation (20) with equation (21):

$$h_{sw}(T_{sed} - T_w) = \frac{\partial}{\partial t} \int_{z_0}^0 C_v T(z) dz + \lambda_s \frac{\partial T}{\partial z} \Big|_{z_0} \quad (22)$$

[27] Regressions were performed at each field location using the full time series of observations (November 2008–September 2009) and by binning the data into  $0.1^\circ\text{C}$   $\Delta T$  bins. Conditions were limited to periods of inundation where the depth was greater than 1 m in order to eliminate the potential interference of solar radiation reaching the bottom of the water column and providing an extra heat source to the sediment bed.

[28] Examples of these regressions are shown in Figure 3 for characteristic sites at both Skagit Bay (Figure 3a) and Willapa Bay (Figure 3b). Values of  $h_{sw}$  for both Skagit and Willapa Bays range from  $2.0$  to  $20 \text{ W m}^{-2} \text{ K}^{-1}$ , depending on the composition of a specific location.  $\Delta H_{sed}$  and  $\Delta T$  were well correlated at both sites with  $r^2 = 0.86$  for Skagit Bay and  $r^2 = 0.85$  for Willapa Bay.

### 3. Results

[29] Each location was modeled for 15–20 days during the winter and summer months in order to observe the spring-neap tidal cycle. Model time periods were based on observational time periods. The summer model time period

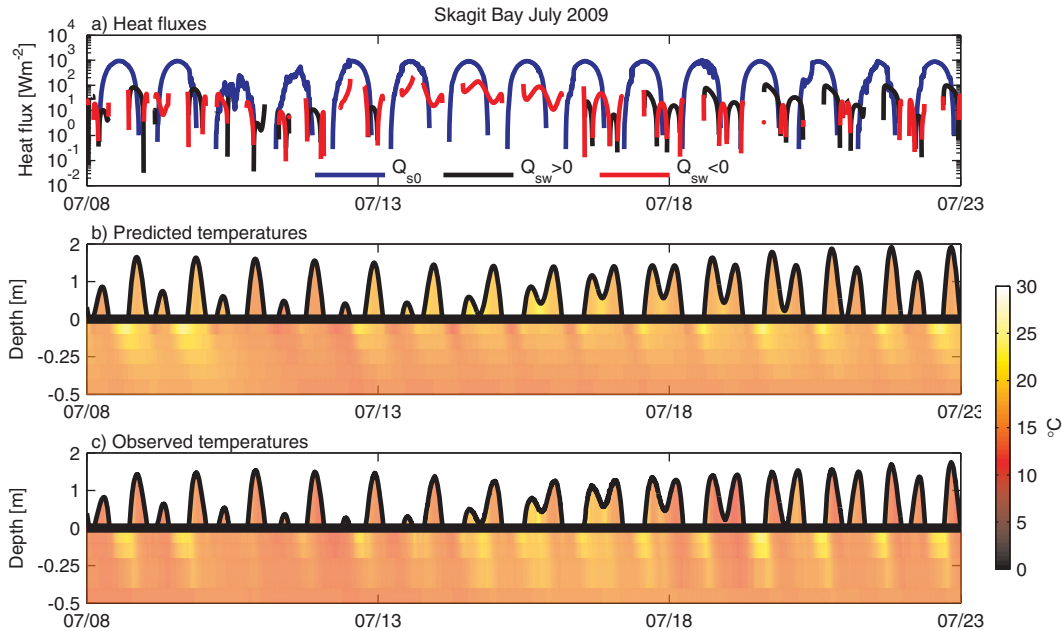


**Figure 4.** Modeled and observed results for 9–24 July 2009 at Skagit Bay S13. (a) Observed incoming shortwave radiation  $Q_{s0}$  (blue) and modeled sediment-water heat fluxes  $Q_{sw}$  (red/black). Black lines indicate positive (into water) fluxes, while red lines are negative (into sediment) fluxes. (b) Modeled and (c) observed sediment and water column temperatures. The sediment bed is represented by negative depths and is exaggerated by a factor of four.

for Skagit Bay was from 7 to 27 July 2009 and the winter period was from 9 to 29 January 2009. For Willapa Bay, the summer modeled time period was from July 2009 and, due to the unavailability of winter data, the “winter” run was during March 2009.

[30] Figure 4 shows the observations and model results of water and sediment temperatures for Skagit Bay during summer 2009 (9–24 July). The strong summer solar shortwave radiation drives the sediment and water column temperatures during this time period. A fortnightly signal is evident, which is specific to the seasonal modulation of tidal phasing in the Pacific Northwest. During the spring tides (9–11 and 21–23 July), exposure of the seabed occurs during the day causing the surface of the flats to absorb the incident solar radiation and heat up. The heat then diffuses vertically down into the sediment. When the site becomes inundated, with cooler water above the surface of the flats, heating stops and the sediment cools as heat is conducted into the water column (i.e.,  $Q_{sw}$  positive). During the neap tides (13–18 July), daytime exposures are brief and hence the sediments do not warm up. Instead the water column absorbs the solar shortwave radiation and  $Q_{sw}$  is then directed into the sediment. These sediment-water heat fluxes are generally 10–20% of the incoming solar shortwave radiation.

[31] The tidal phasing is reversed in the winter and net cooling occurs, as shown in Figure 5. During the winter spring tides, tidal flat exposure occurs at night when no solar shortwave radiation is incident on the flats. This exposure leads to cooling of the sediments and the subsequent inundation of warmer water over cold flats. Sediment-water heat fluxes are then directed toward the sediment bed during this entire time period. These sediment-water heat

fluxes are generally of the same order as the solar shortwave fluxes and are important after sunset when shortwave input vanishes.

[32] For both seasons, the model accurately represents the sediment temperatures. The root-mean-square errors (RMSE) in sediment temperature are 2.72 and 3.98°C for the summer and winter, respectively. The RMSE in water temperatures is 2.54°C for the summer; no water temperature data were available for the winter. These errors are small relative to the 20°C diurnal variations. The model is unable to reproduce some of the higher frequency variability (e.g., during the summer neap tides 13–18 July). This is likely due to circulation and along-flat variations, including changes in offshore temperature and river input.

[33] Similar patterns are apparent at the Willapa Bay site for summer (21–28 July), as shown in Figure 6. Strong solar shortwave radiation heats up the exposed flats during summer low tides. The Willapa site has greater exposure during the smaller semidiurnal tide than the Skagit site due to the larger diurnal inequality in Puget Sound than on the coast. Minimal cooling occurs during these smaller tides, however, and the dominate summer signal is the heating of the tidal flats. During the late winter (2–22 March), shown in Figure 7, nighttime cooling dominates the sediment temperatures causing sediment-water fluxes to be directed toward the sediment bed. Model RMSEs are 4.46 and 2.9°C for the summer and winter water temperatures and 3.56 and 0.96°C for the summer and winter sediment temperatures, respectively. Despite the similar magnitude of  $Q_{s0}$  during July and March,  $Q_{sw}$  is directed into the sediment bed (from the water) for most of the winter results, because the exposure of the flats and high daytime shortwave radiation are out of phase.

RINEHIMER AND THOMSON: TIDAL FLAT HEAT FLUXES

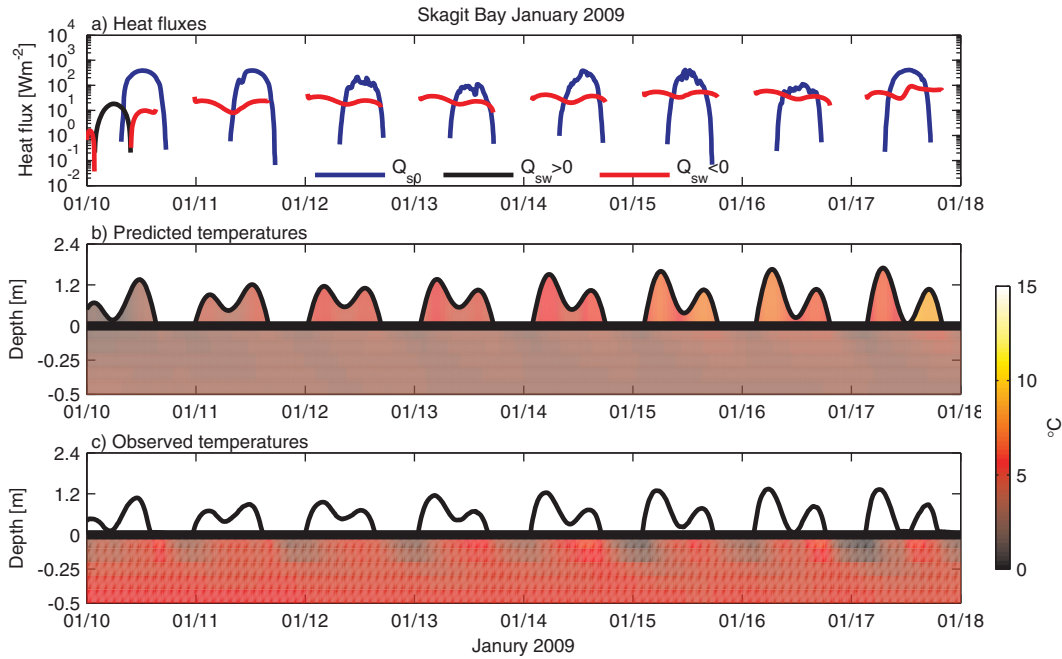


**Figure 5.** Modeled and observed results for 10–20 January 2009 at Skagit Bay S13. (a) Observed incoming shortwave radiation  $Q_{s0}$  (blue) and modeled sediment-water heat fluxes  $Q_{sw}$  (red/black). Black lines indicate positive (into water) fluxes, while red lines are negative (into sediment) fluxes. (b) Modeled and (c) observed sediment temperatures. The sediment bed is represented by negative depths and is exaggerated by a factor of four. Water column observations were unavailable for this period.

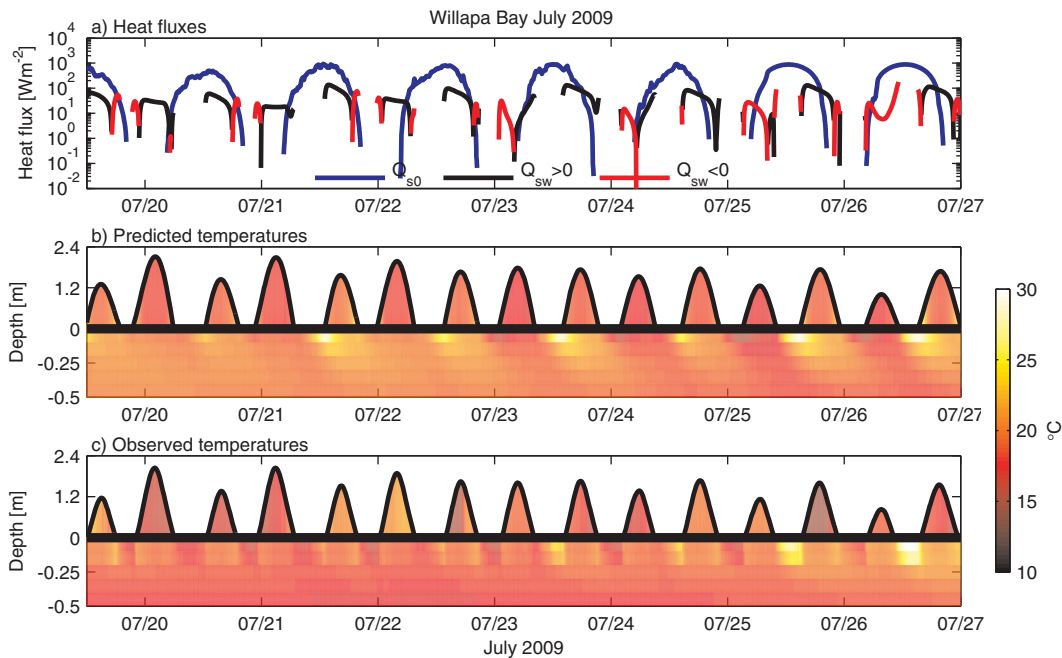


**Figure 6.** Modeled and observed results for 21–28 July 2009 at Willapa Bay W02. (a) Observed incoming shortwave radiation  $Q_{s0}$  (yellow) and modeled sediment-water heat fluxes  $Q_{sw}$  (red/black). Black lines indicate positive (into water) fluxes, while red lines are negative (into sediment) fluxes. (b) Modeled and (c) observed sediment and water column temperatures. The sediment bed is represented by negative depths and is exaggerated by a factor of four.

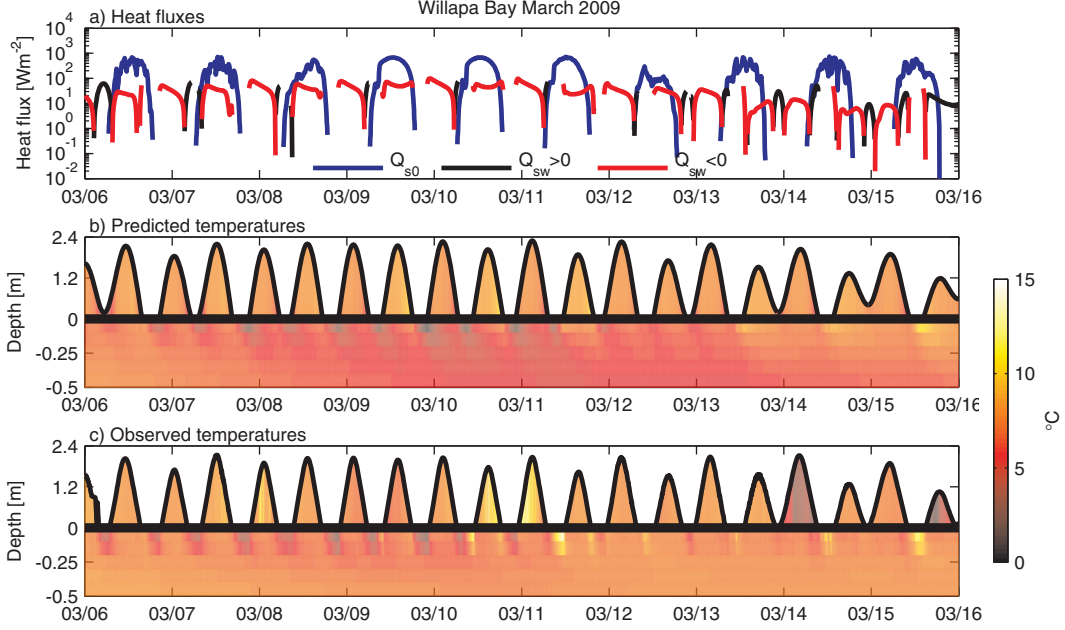


**Figure 7.** Modeled and observed results for 6–16 March 2009 at Willapa Bay W02. (a) Observed incoming shortwave radiation  $Q_{s0}$  (yellow) and modeled sediment-water heat fluxes  $Q_{sw}$  (red/black). Black lines indicate positive (into water) fluxes, while red lines are negative (into sediment) fluxes. (b) Modeled and (c) observed sediment and water column temperatures. The sediment bed is represented by negative depths and is exaggerated by a factor of four.

### 3.1. Influence of Solar-Tidal Phasing on Sediment-Water Heat Transfer

[34] To further examine the relationship between flat exposure times and daily solar radiation, the parameter  $\Delta T_{\text{MLLW}}$  was defined as:

$$\Delta T_{\text{MLLW}} = T_{\text{solar noon}} - T_{\text{MLLW}} \quad (23)$$

where  $T_{\text{MLLW}}$  is the time of mean-lower-low water (MLLW) and  $T_{\text{solar noon}}$  is the time of local solar noon. Negative values of  $\Delta T_{\text{MLLW}}$  indicate solar noon occurring before MLLW while if local solar noon follows MLLW,  $\Delta T_{\text{MLLW}}$  is positive. The daily mean total sediment-water heat fluxes  $\bar{q}_{sw}$  were determined by

$$\bar{q}_{sw} = \frac{1}{L_x} \int_0^{L_x} \int_{\text{daily}} Q_{sw}(t, x) dt dx \quad (24)$$

where the time integral is taken over each day.  $\bar{q}_{sw}$  represents the mean of the total sediment-water heat transfer over all the cross-flat locations. Daily values of  $\Delta T_{\text{MLLW}}$  and  $\bar{q}_{sw}$  are shown in Figure 8 for each site and season.

[35] As the difference in time between MLLW and solar noon increases, sediment-water heat transfer falls and becomes directed from the water column to the sediment. The highest total sediment-water heat transfers occur when  $\Delta T_{\text{MLLW}}$  is about 1–2 h following local solar noon. This lag is likely explained by local meteorological conditions. While the potential shortwave radiation is at a maximum at local solar noon, daily air temperatures, which control loss of heat from the sediment surface through longwave, latent, and sensible fluxes, do not peak until later in the day. Addi-

tionally, the lag is more apparent during the summer months when a shallow marine layer generates morning cloudiness which generally gives way to clear skies by the afternoon. This diurnal cloudiness variation would strongly

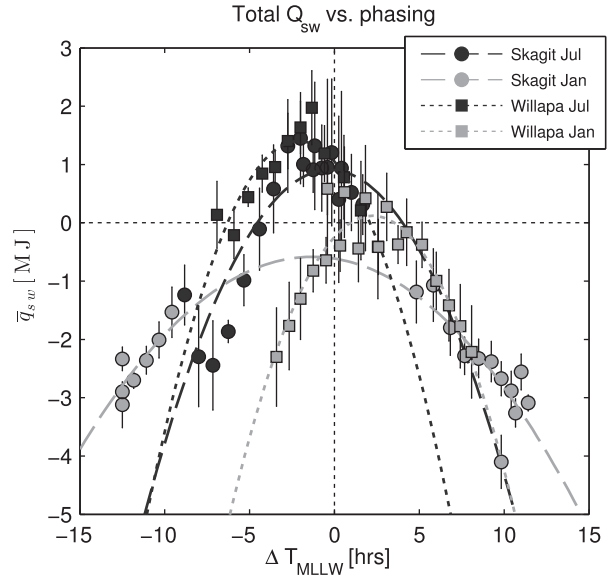


**Figure 8.** Modeled mean daily total sediment-water heat transfer  $\bar{q}_{sw}$  versus the time difference between MLLW and local solar noon  $\Delta T_{\text{MLLW}}$ . Skagit Bay sites are circles and Willapa Bay sites are squares. Summer is in black and winter in gray. The error bars are the standard deviation over all the modeled  $x$  locations while the curves are least-squares fit lines using a second-order polynomial.

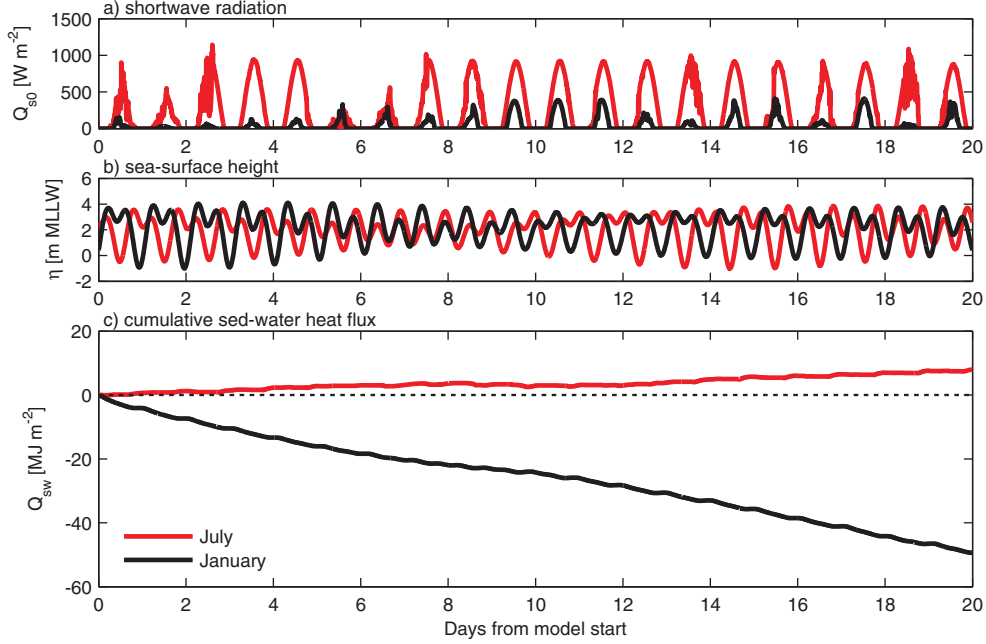


**Figure 9.** Modeled (a) solar shortwave radiation, (b) sea-surface height, and (c) cumulative sediment-water heat fluxes for July (red lines) and January (black lines) 2009 at Skagit Bay S13.

inhibit morning solar shortwave radiation and the subsequent increase in heat uptake by the exposed flats. In either case, MLLW occurrence during the morning would be less effective at storing heat than afternoon exposure.

[36] The seasonality of the phasing is also apparent in Figure 8 as the summer  $\Delta T_{\text{MLLW}}$  is concentrated from  $-5$  to  $2$  h while winter  $\Delta T_{\text{MLLW}}$  ranges between  $\pm 12$  h. Interestingly, the range of the daily mean total sediment-water heat transfer,  $\bar{q}_{sw}$ , seems independent of season with values between  $\pm 3$  MJ during both seasons at each site. Willapa Bay during the summer is an exception with a negative  $\bar{q}_{sw}$  occurring only once, however, this may just be due to the lack of data as  $\Delta T_{\text{MLLW}}$  during Willapa summer does not fall outside of  $-7$  to  $2$  h where negative  $\bar{q}_{sw}$  would be expected.

### 3.2. Cumulative Heat Fluxes by Season

[37] To determine the long-term influence of sediment-water heat fluxes on the water column,  $Q_{sw}$  was integrated over each of the modeled periods for the summer and winter cases. The cumulative heat fluxes for Skagit Bay are shown in Figure 9. During the summer, the sediment acts as a minor net source of heat to the water column, providing about  $5 \text{ MJ m}^{-2}$  of heat over a fortnight. During the winter, however, the sediment bed is a net sink, absorbing about  $-25 \text{ MJ m}^{-2}$  of heat over a fortnight. The relationship between the phasing of the exposure of the flats and the incident shortwave radiation is clearly seen in plots (a) and (b) of Figure 9.

[38] While the net  $Q_{sw}$  is slightly positive (from the sediment to the water) during the summer, the fluxes are modulated by the tidal signal: positive during spring tides and negative during neap tides. During spring tides maximum exposure and solar radiation are in phase, while during neap tides minimum exposure and solar radiation are in phase. Each tidal cycle, heat is transferred to or lost from

the water at high tide depending on the conditions of the previous low tide. The opposite fortnightly signal is evident during the winter, and the net effect is a loss of heat from the water column to the sediment surface.

[39] The effects of the coincidence of flat exposure and daytime solar radiation are even more apparent at Willapa Bay, as shown in Figure 10. Incident shortwave radiation during March is 70% of the July values, because it is late in the winter, but the seasonal difference is still evident. The net cumulative heat flux during the July fortnight is only about  $+2 \text{ MJ m}^{-2}$ , while net cumulative heat flux during the March fortnight is about  $-25 \text{ MJ m}^{-2}$ . Thus, phasing appears to be a stronger control on cumulative fluxes than the magnitude of solar radiation.

### 3.3. Heat Fluxes at the Leading Edge of the Flood Front

[40] During the summer period at Skagit Bay, observed water column temperatures immediately after inundation are  $\approx 5^\circ\text{C}$  warmer than the sediment surface temperatures. Figure 11 shows this phenomena by tidally phase-averaging temperatures, using time after inundation, from 13 to 18 July at Skagit Bay and 21 to 28 July at Willapa Bay. These time periods were chosen as they represent the period of maximum exposure at these sites and hence the strongest signals for heating at the leading edge. These leading edge water temperatures exceed the sediment temperatures at both up-flat and down-flat locations, implying that the source of heat cannot be from the sediment. The most likely mechanism is solar heating, which for a thin fluid is a strong function of absorption.

[41] To examine the effects of solar absorption at the leading edge of the flooding front, the thermodynamic model was run for two different light extinction coefficients:  $K_d = 1 \text{ m}^{-1}$  and  $K_d = 1000 \text{ m}^{-1}$ . Model results are included in Figure 11, in which the high  $K_d$  values

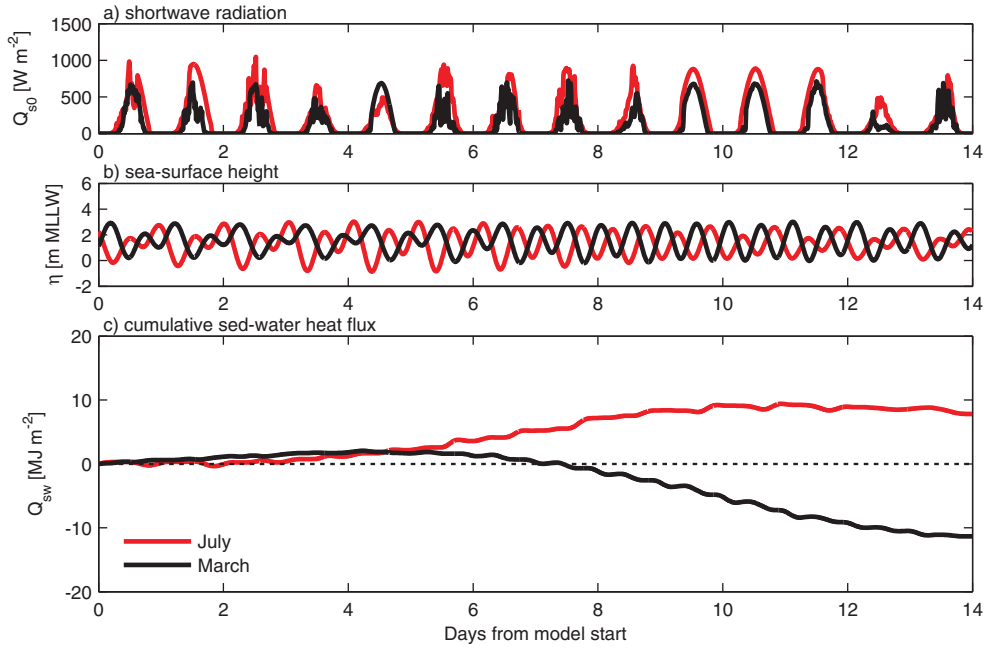


**Figure 10.** Modeled (a) solar shortwave radiation, (b) sea-surface height, and (c) cumulative sediment-water heat fluxes for July (red lines) and March (black lines) 2009 at Willapa Bay S02.

successfully reproduce the general trend of the data. In particular, high  $K_d$  values cause the thin leading edge of flooding water to warm well above the sediment temperatures. In contrast, low  $K_d$  values do not reproduce the leading edge temperature.

[42] The effect of solar absorption is most evident in the 20 min ( $\approx 0.3$  h) after the inundation, when water column

temperatures are  $4^\circ\text{C}$  greater during the high  $K_d$  runs. However, the high value of  $K_d$  also is important for reproducing the correct sediment temperatures at longer times. This is because any solar radiation not absorbed by the water will go into the sediment. For example, at Skagit Bay, the low  $K_d$  values result in a spurious warming of the sediments. This spurious warming creates an accumulating bias in the

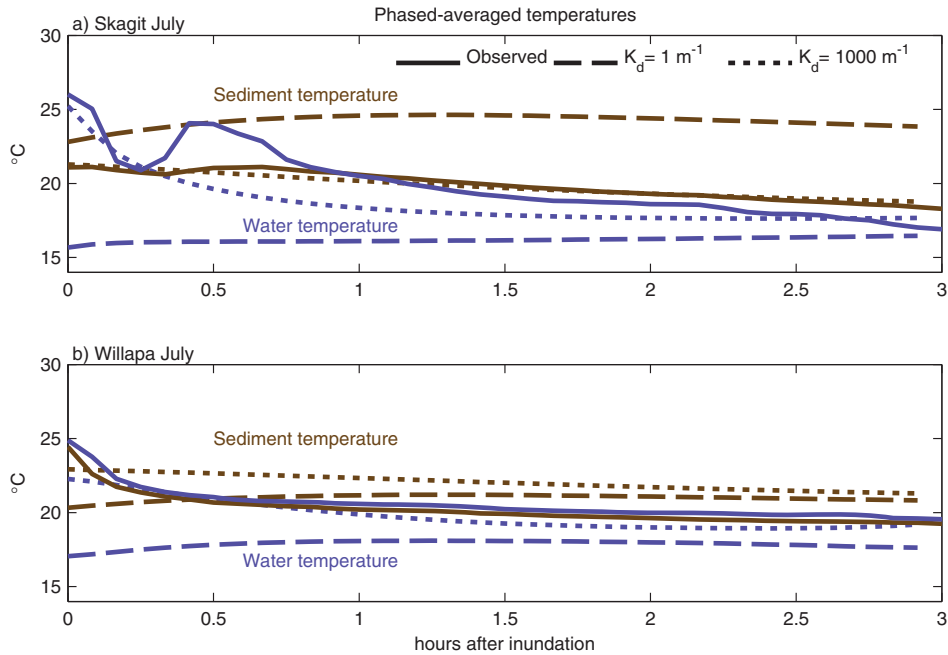


**Figure 11.** Tidally phase-averaged water (blue) and sediment (brown) surface temperatures for (a) 13–18 July 2009 at Skagit Bay and (b) 21–28 July 2009 at Willapa Bay. The x axis increases from 0 at the time of inundation to 3 h after inundation. Solid lines are the observed temperatures, dashed lines indicate an extinction coefficient of  $K_d = 1000 \text{ m}^{-1}$ , and dotted lines  $K_d = 10000 \text{ m}^{-1}$ .

**Table 1.** Parameter Values Used for Sensitivity Runs<sup>a</sup>

Parameter	Values Tested
$\kappa$	0.4, 0.8, 1.2 mm <sup>2</sup> s <sup>-1</sup>
$\lambda_s$	3, 5, 8 W m <sup>-1</sup> K <sup>-1</sup>
$H_{sw}$ (Skagit)	10, 15, 20 W m <sup>-2</sup> K <sup>-1</sup>
$H_{sw}$ (Willapa)	5, 10, 15 W m <sup>-2</sup> K <sup>-1</sup>
$T_{sea}$ (Summer)	10, 12, 14 °C
$T_{sea}$ (Winter)	6, 8, 10, 12 °C

<sup>a</sup>Each combination of parameters was tested for a total of 81 “summer” runs and 108 “winter” runs.

model results and dramatically increases the RMSE between model and data. The high value of  $K_d$  is required to match the data over fortnightly periods, and by extension, to correctly infer seasonal cumulative heat fluxes.

[43] The tidal phasing that creates net heating or cooling also amplifies the effect of solar absorption. During neap tides, the flats are preferentially inundated when the solar radiation is largest, and thus high  $K_d$  values notably increase the water temperatures. This is consistent with the observations. For example, at Skagit Bay in the summer, the neap tide water midday temperatures are about 25°C, compared with the spring tide water temperatures at 18°C (see Figure 4).

[44] At Willapa Bay, the high  $K_d$  value is similarly important in matching the observed temperatures at both short and long time scales, however, the water temperature does not exceed the sediment temperature during the initial arrival of the flood (see Figure 11). Rather, the water and sediment are in near-equilibrium most of the time. This is likely related to the much higher water content of the muddy sediments at Willapa Bay, compared with the sandy sediments at Skagit Bay. This contrast in composition is consistent with the Willapa tidal flats having thermal properties much closer to that of water [Thomson, 2010].

### 3.4. Model Skill and Sensitivity to $\lambda_s$ , $H_{sw}$ , $\kappa$ , and $T_{sea}$

[45] Due to the variability and complexity of sediment-water mixtures, bed thermal parameters like the sediment-water heat-transfer coefficient ( $H_{sw}$ ), bulk thermal conductivity ( $\lambda_s$ ), and bulk thermal diffusivity ( $\kappa$ ) are not well constrained. Thomson [2010] found  $\kappa$  to vary between 0.4 and  $1.4 \times 10^{-6}$  m<sup>2</sup> s<sup>-1</sup> while  $\lambda_s$  varied from 1 to 8 W m<sup>-1</sup> K<sup>-1</sup>, both highly dependent on the porosity (i.e., water content) and hence composition of the sediment.  $H_{sw}$  values (as measured in section 2.2.3.) ranged from 2.0 to 20 W m<sup>-2</sup> K<sup>-1</sup>. Additionally, the offshore boundary condition  $T_{sea}$  was also not well constrained as few water temperature observations were available away from the site.

[46] To determine the effects of variations in these parameters on model results, the model was run repeatedly, iterating over all combinations of these parameters (see Table 1). Model-data fit was estimated using the mean error (or bias):

$$ME = \frac{1}{N} \sum_{i=1}^N (f_i - x_i) \quad (25)$$

where  $x_i$  is the observed value at time  $i$ ,  $f_i$  is the predicted value, and  $N$  is the total number of time points to take the mean. As the values in the ME are not squared, it can be used to indicate bias in the model results (i.e., it is the dif-

ference between the model and observational means). ME, however, gives little indication of how well the model fits the data as large positive and negative difference will cancel each other.

[47] Model-data fits were estimated using the model skill [Murphy, 1988]:

$$S = 1 - \frac{MSE_{model}}{MSE_{ref}} \quad (26)$$

where  $MSE_{model} = \frac{1}{N} \sum_{i=1}^N (f_i - x_i)^2$  is the mean-squared error of the model and  $MSE_{ref}$  is the mean-squared error of some reference forecast to which the current model is compared. The simplest reference forecast is the mean  $\bar{x}$  of the data set which using  $MSE(\bar{x}) = \sigma^2(x)$  gives:

$$S = 1 - \frac{MSE_{model}}{\sigma^2(x)} \quad (27)$$

where  $\sigma^2(x)$  is the variance of the time series. Negative skill scores indicate that the model does worse than the reference forecast, positive scores indicate the model does better while  $S = 1$  indicates a perfect forecast.

[48] Skill estimates were computed for the time-varying water temperature and for the sediment temperatures (for all observed depths). The sensitivity model runs indicate that for certain sets of parameter values, the model does better than a simple statistical prediction of temperatures by the mean. The most variation was seen in the model parameter  $T_{sea}$ , the offshore boundary condition. Due to this, a single value of  $T_{sea}$  was chosen for each of the four site and seasons combinations for presentation and analysis. Ideally,  $T_{sea}$  would be set with either observed conditions or a large-scale model.

[49] Values of skill and ME for each of the runs are presented in Figure 12 for Skagit Bay and Figure 13 for Willapa Bay. Table 2 shows the most skillful set of model parameters for each site and season as determined by the maximum of the sum of the water and sediment skill values. At Skagit Bay in the summer, water temperatures are biased low while sediment temperatures are biased high. As  $H_{sw}$  and  $\lambda_s$  increase, water temperatures become less biased and the skill approaches 0.38. Sediment temperatures show similar pattern, but skill increases the greatest as  $\kappa$  increases. For the winter time period at Skagit Bay, water temperature observations were unavailable. Sediment temperatures show increasing skill as  $\lambda_s$  increases and minimal bias for the middle value of  $H_{sw} = 10$  W m<sup>-2</sup> K<sup>-1</sup>.

[50] At Willapa Bay, skills are generally lower than at Skagit Bay and only reach about 0.14 and 0.20 for the water and sediment in March and 0.11 for both the water and sediment in July. Similar to the Skagit Bay data, water column skills are greater as  $H_{sw}$  and  $\lambda_s$  increase. In the sediment bed, increasing  $\kappa$  reduces the bias for both the winter and summer runs.

## 4. Discussion

### 4.1. Hydrodynamic Effects

[51] As both of these tidal flats are located in estuarine environments, there is potential for strong vertical

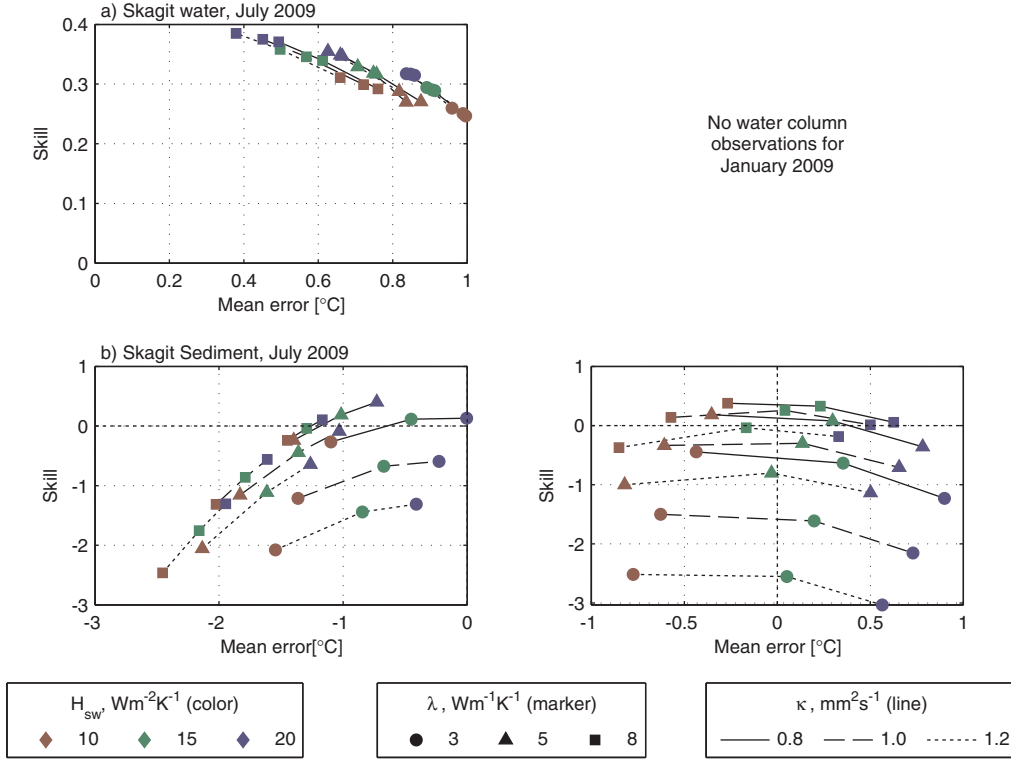


**Figure 12.** Mean error and skill scores for Skagit Bay water temperatures during (a) July 2009 and sediment temperatures during (b) July 2009 and (c) January 2009. Colors represent various  $H_{sw}$  values: (red) 5, (green) 10, and (blue) 15  $W m^{-2} K^{-1}$ . Markers indicate changes in  $\lambda_s$ : (circle) 3, (triangle) 5, and (square) 8  $W m^{-1} K^{-1}$ . Black lines connect values with the same  $\kappa$  value: (solid) 0.8, (dashed) 1.0, and (dotted) 1.2  $mm^{-2} s^{-1}$ . For July,  $T_{sea} = 14^\circ C$  and for January,  $T_{sea} = 10^\circ C$ . No water-column observation data were available for Skagit Bay in January 2009. Note the change in y axis limits for each plot.

variations in salinity, especially at Skagit Bay where the flats are essentially a subaqueous tidal river delta. Strong vertical salinity gradients have been observed in shallow ( $<5$  m) water in similar tidal flats in San Francisco Bay [Ralston and Stacey, 2005] as well as at the Skagit Bay site [Pavel et al., 2012]. These salinity gradients would inhibit vertical mixing and invalidate the 1-D assumption of a vertically well-mixed water column. This would reduce the heat transfer between the surface layers and the bed layers, uncoupling the seabed from the water column. As strength of the salinity gradient increases, its spatial, and also temporal, range would decrease. This implies that as stratification increases, its long-term effects on the heat budget decrease as, most of the time, the water column would be relatively homogeneous and would only experience stratification occasionally. While instantaneous temperatures would be altered, the long-term trends would likely be similar.

[52] In the skill assessment,  $T_{sea}$  affected the greatest variability in model skill. The chosen value for  $T_{sea}$  determined the “baseline” water temperature and, therefore, even  $2^\circ C$  changes significantly altered model-data comparisons. The choice of a constant value for each run was based on the lack of local observations of “offshore” temperatures for these time periods. For the short time periods modeled in this study, the constant  $T_{sea}$  values were sufficient, but long-term measurements would be required to accurately model annual changes or climate scenarios.

## 4.2. Choice of Skill-Assessment Parameters

[53] The choice of the skill-assessment parameters ( $T_{sea}$ ,  $\kappa$ ,  $\lambda$ ,  $H_{sw}$ ) was intended to focus on the sediment characteristics, particularly those that are least well constrained.  $T_{sea}$ , while not a sediment parameter, was included as it has a substantial effect on model results and large variability over the model time periods, however, as outlined above, was eventually used as a “tuning” parameter. The results of the skill scores (Figures 12 and 13) do not exhibit a “maxima-like” behavior around a particular parameter set indicating that more appropriate values are outside the range of those tested. As our choice of parameter values, particularly  $\kappa$  and  $\lambda$  span the range observed in field data [Thomson, 2010], using parameters outside of these values would be unjustified by the observations.

[54] One important parameter not included in the sensitivity tests was the albedo,  $\alpha_s$  and  $\alpha_w$ . The winter sediment temperatures are biased low with lower than observed temperatures particularly strong during periods of exposure. This indicates that net heat fluxes during exposed periods are underpredicted. Overestimation of reflected shortwave by high albedo values would be one potential mechanism for generating a low bias.

[55] Other sources of a low sediment temperature bias include inaccurate estimation of clouds. This is especially true at the Willapa Bay site where the cloud data used were from the Astoria airport. While Astoria is within 50 km of

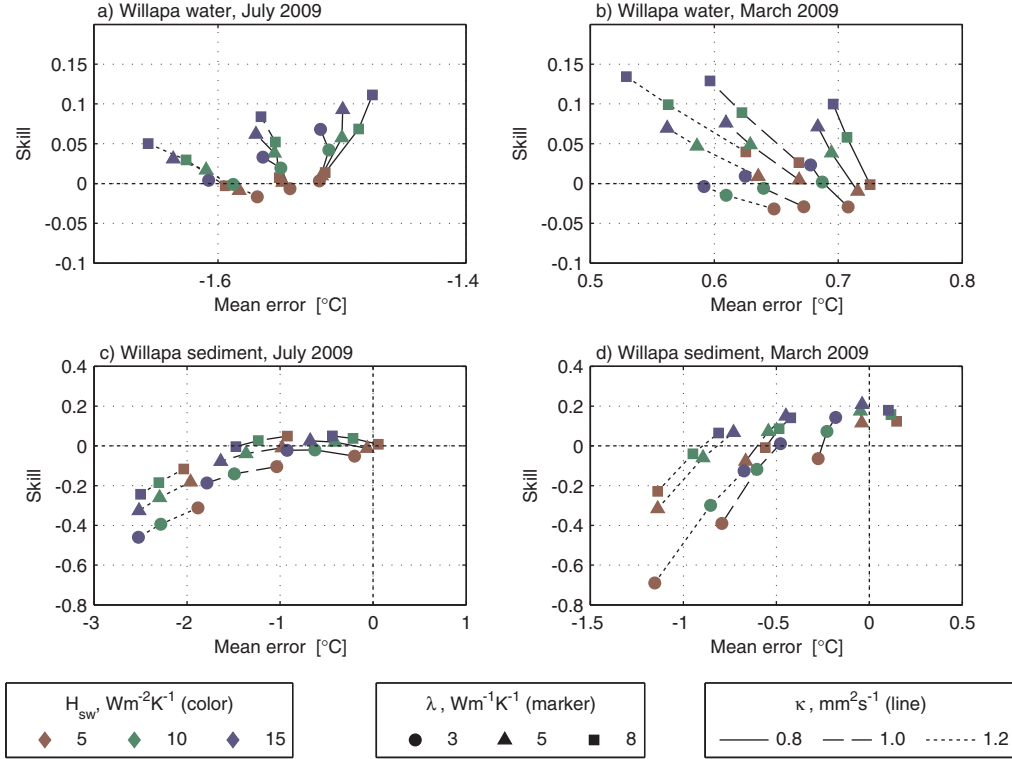


**Figure 13.** Mean error and skill scores for Willapa Bay water temperatures during (a) July 2009 and (b) March 2009 and sediment temperatures during (c) July 2009 and (d) January 2009. Colors represent various  $H_{sw}$  values: (red) 5, (green) 10, and (blue) 15  $W m^{-2} K^{-1}$ . Markers indicate changes in  $\lambda_s$ : (circle) 3, (triangle) 5, and (square) 8  $W m^{-1} K^{-1}$ . Black lines connect values with the same  $\kappa$  value: (solid) 0.8, (dashed) 1.0, and (dotted) 1.2  $mm^{-2} s^{-1}$ .  $T_{sea} = 15^\circ C$  in July and  $T_{sea} = 8^\circ C$  in March. Note the change in y axis limits for each plot.

Willapa Bay, the nearby Columbia river and hills south of the bay alter local meteorology significantly such that Astoria may experience more sunny days than Willapa Bay. If the cloud cover was underpredicted, more longwave radiation would be lost, especially during the winter months, causing a net low predicted temperature. Alternatively, the formula for longwave radiation [May, 1986] may not be suitable for sediment beds as it was developed for surface water temperatures.

[56] Sediment surface processes during exposure could also create bias in the model results. Desiccation of the upper millimeter would alter bulk thermal properties like  $\kappa$  and  $\lambda_s$ . Strong temperature gradients occur within the upper millimeter of the sediment and would not be resolved by the model. As the surface temperature controls the transfer of heat through all fluxes but shortwave, not accurately resolving the temperature could cause misprediction of

these fluxes. For example, overprediction of surface temperatures could cause overprediction of emitted longwave radiation and hence a bias toward low temperatures.

#### 4.3. Relationship Between $K_d$ and Turbidity

[57] High  $K_d$  values are necessary to accurately model the post-inundation water and sediment temperatures. The strong absorption of solar radiation is consistent with visual observations (in the field) of extremely high turbidity, especially in the first stage of the flood. Aerial photos from Skagit flats, in particular, have shown a leading edge of turbid water, often repeated by a second line of turbid water. This likely is related to the second peak in water temperature 0.5 h after inundation at Skagit Bay (see Figure 11). Such heterogeneity is not captured in the model, which uses a constant  $K_d$ . It is likely that along flat convergence during the flood tide or the effects of river outflow, processes not

**Table 2.** Most Skillful Model Parameters for Each Site and Season Determined as the Sum of Both Water and Sediment Skill Values

		$\lambda_s$ ( $W m^{-1} K^{-1}$ )	$H_{sw}$ ( $W m^{-2} K^{-1}$ )	$T_{sea}$ ( $^\circ C$ )	$\kappa$ ( $mm^2 s^{-1}$ )	Water		Sediment	
						ME ( $^\circ C$ )	Skill	ME ( $^\circ C$ )	Skill
Skagit	July	5	20	14	0.8	0.66	0.35	-0.72	0.40
	January	8	10	12	0.4			-0.27	0.38
Willapa	July	8	15	15	0.4	-1.5	0.11	-0.44	0.05
	March	8	15	8	0.8	0.60	0.13	-0.42	0.14

included in the model, create a double peak in turbidity that causes enhanced absorption of shortwave radiation. Although these details are not captured, the model does identify the mechanism of solar absorption in water as controlling much of the thermodynamics.

[58] The high  $K_d$  value used replicate the enhanced water temperatures of the advancing flood are an order of magnitude above the greatest values ( $100 \text{ m}^{-1}$ ) reported for just the infrared portion of the incoming radiation. Most observations of light extinction coefficient occur in water depths 0(1–10 m) where back-radiation of shortwave energy is less than 1% of the incoming radiation [Stefan *et al.*, 1983]. Considering the extremely shallow, centimeter scale flows that occur at the edge of the flooding front, it is likely that back-radiation and reabsorption of shortwave radiation occurs causing the simple one-directional model of equation (11) to underpredict the fraction of shortwave radiation absorbed by the water column and hence require larger extinction coefficients.

## 5. Conclusion

[59] A simple model of cross-shore tidal flat heat transport captures the basic patterns of temperature variations in both the water column and sediment bed for muddy and sandy sites during winter and summer months. Sediment-water heat fluxes are an important component of the heat budget, representing up to 20% of the incoming solar radiation and being larger than latent and sensible heat fluxes. The phasing of tidal flat exposure and daylight is important in controlling the sediment-water heat exchange. During the summer months, net heat flux is from the sediment bed to the water column as the longest periods of exposure occur during the daytime and result in the uptake of heat by the tidal flats. The heat stored in the flats is then released to the water column during inundation. Under winter conditions, the phasing is reversed with maximum flat exposure occurring during the nighttime, causing a loss of heat to the atmosphere and a net transfer of heat from the water column to the sediment.

[60] The model reproduces temperature observations on tidal, fortnightly, and seasonal time scales. On tidal time scales, a controlling process is the absorption of the shortwave radiation by water. Consistent with observations of high turbidity, the absorption must be near-total for the model to match the temperature observations. The high water temperatures of the initial flooding front create subsequent negative values of  $Q_{sw}$  (i.e., heat going from water to sediment). After passage of the initial front, however, sediment-water heat transfer reverses, with the water gaining heat from the sediment bed. Without high extinction coefficients, the shortwave radiation is transmitted through the shallow water column and absorbed by the seabed. This incorrectly heats the sediments instead of the water.

[61] The net heat budget of coastal regions controls water and seabed temperatures which drive rates of biogeochemical processes as well as local climate. While the net  $Q_{sw}$  is small compared to solar shortwave radiation, it is of the same order as the net  $Q_w$  highlighting its importance. The effects of inundation and exposure in coastal systems provide an additional pathway for heat and mass transfers in this transitional environment. Understanding the details of

these processes is imperative as sea level rise and human alterations modify coastlines and the nearshore environment.

[62] **Acknowledgments.** A. deKlerk designed, built, tested, and deployed the sediment temperature profilers. A. de Klerk, A. Ogston, C. Nittrouer, K. Lee, R. Hale, T. Drexler, C. Chickadel, Talbert, and D. Pollard assisted in field deployment and recovery. Thanks to C. Chickadel and A. Horner-Devine for comments on the manuscript. Washington State University AgWeatherNet provided supplemental meteorological data used for the model. Funding provided by Office of Naval Research grant N000141010215.

## References

- Amos, C. L. (1995), *Siliclastic tidal flats, in Geomorphology and Sedimentology of Estuaries*, edited by G. M. E. Perillo, pp. 273–306, Elsevier, Amsterdam.
- Andrews, R. (1965), Modern sediments of Willapa Bay, Washington: A coastal plain estuary, *Tech. Rep. 118*, Dep. of Oceanogr., Univ. of Wash, Seattle, Wash.
- Boldt, K. V., C. A. Nittrouer, and A. S. Ogston (2013), Seasonal transfer and net accumulation of fine sediment on a muddy tidal flat: Willapa Bay, Washington, *Cont. Shelf Res.*, 60, S157–S172, doi:10.1016/j.csr.2012.08.012.
- Cahill, B., O. Schofield, R. Chant, J. Wilkin, E. Hunter, S. Glenn, and P. Bissett (2008), Dynamics of turbid buoyant plumes and the feedbacks on near-shore biogeochemistry and physics, *Geophys. Res. Lett.*, 35, L10605, doi:10.1029/2008GL033595.
- Cho, Y.-K., M.-O. Kim, and B.-C. Kim (2000), Sea fog around the Korean Peninsula, *J. Appl. Meteorol.*, 39(12), 2473–2479.
- Colijn, F., and V. de Jonge (1984), Primary production of microphytobenthos in the Ems-Dollard Estuary, *Mar. Ecol. Prog. Ser.*, 14(2), 185–196.
- Friedrichs, C. T. (2012), Tidal flat morphodynamics: A synthesis, in *Treatise on Estuarine and Coastal Science*, vol. 3, pp. 137–170, Elsevier, London, doi:10.1016/B978-0-12-374711-2.00307-7.
- Guarini, J., G. Blanchard, P. Gros, and S. Harrison (1997), Modelling the mud surface temperature on intertidal flats to investigate the spatio-temporal dynamics of the benthic microalgal photosynthetic capacity, *Mar. Ecol. Prog. Ser.*, 153, 25–36, doi:10.3354/meps153025.
- Harrison, S. (1985), Heat exchanges in muddy intertidal sediments: Chichester harbour, West Sussex, England, *Estuarine Coastal Shelf Sci.*, 20(4), 477–490, doi:10.1016/0272-7714(85)90090-3.
- Incropera, F. P., and D. P. DeWitt (2002), *Introduction to Heat Transfer*, 4th ed., John Wiley, New York.
- Jerlov, N. G. (1976), *Marine Optics*, Elsevier, Amsterdam.
- Kim, T.-W., Y.-K. Cho, and E. P. Dever (2007), An evaluation of the thermal properties and albedo of a macrotidal flat, *J. Geophys. Res.*, 112, C12009, doi:10.1029/2006JC004015.
- Kim, T.-W., Y.-K. Cho, K.-W. You, and K. T. Jung (2010), Effect of tidal flat on seawater temperature variation in the southwest coast of Korea, *J. Geophys. Res.*, 115, C02007, doi:10.1029/2009JC005593.
- Losordo, T. M., and R. H. Piedrahita (1991), Modelling temperature variation and thermal stratification in shallow aquaculture ponds, *Ecol. Modell.*, 54(3–4), 189–226, doi:10.1016/0304-3800(91)90076-D.
- May, P. W. (1986), A brief explanation of Mediterranean heat and momentum flux calculations, *Tech. Rep. NORDA Code 322*, Nav. Ocean Res. and Dev. Activ., Natl. Space Technol. Lab. Stn., Miss. NSTL Station, Miss.
- McBride, A., K. Wolf, and E. Beamer (2006), *Skagit Bay Nearshore Habitat Mapping*, Skagit River Syst. Coop., LaConner, Wash.
- Murphy, A. H. (1988), Skill scores based on the mean square error and their relationships to the correlation coefficient, *Mon. Weather Rev.*, 116, 2417–2424.
- Pavel, V., B. Raubenheimer, and S. Elgar (2012), Processes controlling stratification on the northern Skagit Bay tidal flats, *Cont. Shelf Res.*, 60, S30–S39, doi:10.1016/j.csr.2012.06.012.
- Ralston, D., and M. Stacey (2005), Stratification and turbulence in subtidal channels through intertidal mudflats, *J. Geophys. Res.*, 110, C08009, doi:10.1029/2004JC002650.
- Stefan, H. G., J. J. Cardoni, F. R. Schiebe, and C. M. Cooper (1983), Model of light penetration in a turbid lake, *Water Resour. Res.*, 19, 109–120.
- Thomson, J. M. (2010), Observations of thermal diffusivity and a relation to the porosity of tidal flat sediments, *J. Geophys. Res.*, 115, C05016, doi:10.1029/2009JC005968.
- Yanagi, T., K. Sugimatsu, H. Shibaki, H.-R. Shin, and H.-S. Kim (2005), Effect of tidal flat on the thermal effluent dispersion from a power plant, *J. Geophys. Res.*, 110, C03025, doi:10.1029/2004JC002385.